Detailed investigation of subgrid scale models in large-eddy simulation using high aspect-ratio grid spacing

Abe, Ken-ichi
Department of Aeronautics and Astronautics, Faculty of Engineering, Kyushu University

Ken-ichi Abe (安倍 賢一)

View Online   Export Citation   CrossMark

ARTICLES YOU MAY BE INTERESTED IN

Turbulent characteristics and energy transfer in the far field of active-grid turbulence
Physics of Fluids **33**, 115119 (2021); https://doi.org/10.1063/5.0070912

Da Vinci's observation of turbulence: A French-Italian study aiming at numerically reproducing the physics behind one of his drawings, 500 years later
Physics of Fluids **33**, 115122 (2021); https://doi.org/10.1063/5.0070984

A leading-edge vortex initiation criteria for large amplitude foil oscillations using a discrete vortex model
Physics of Fluids **33**, 115123 (2021); https://doi.org/10.1063/5.0065097

Detailed investigation of subgrid scale models in large-eddy simulation using high aspect-ratio grid spacing

Ken-ichi Abe (安倍 賢一)[a] (iD)

AFFILIATIONS

Department of Aeronautics and Astronautics, Kyushu University, 744, Motooka, Nishi-ku, Fukuoka 819-0395, Japan

[a]Author to whom correspondence should be addressed: abe@aero.kyushu-u.ac.jp

ABSTRACT

In large eddy simulation (LES), we generally use information of the grid width in representing a filter width (Δ) to evaluate a subgrid scale (SGS) model. In practical applications, however, the grid widths are largely different in the streamwise and cross-streamwise directions, resulting in grid cells having high aspect ratios. In such a case, we often adopt the cube root of the grid-cell volume for the filter width; i.e., $\Delta = (\Delta x \Delta y \Delta z)^{1/3}$ in the Cartesian grid system. Although this has been regarded as a standard way to determine the filter width, its superiority over other strategies, such as using the maximum width in all directions (i.e., $\Delta = \max(\Delta x, \Delta y, \Delta z)$), has not always been made clear. In this paper, to investigate the effect of the definition of a filter width on the prediction accuracy of an SGS model, we report on *a priori* tests of several SGS models using highly resolved LES data of a backward-facing step flow. We focus particularly on the model performance in the shear layer downstream of a step, where there exists a strong velocity gradient and the aspect ratio of a grid cell is high despite the region being far from wall surfaces. This investigation enables us to distinguish the effect of the grid aspect ratio from that of near-wall damping. We make the important finding that the cube root of a grid-cell volume is not always appropriate for the filter width. To evaluate an SGS model properly, the effect of a grid width in one direction much smaller than in other directions must be excluded in determining the filter width.

Published under an exclusive license by AIP Publishing. https://doi.org/10.1063/5.0070183

I. INTRODUCTION

In large eddy simulation (LES), the flow variables are decomposed into a directly resolved grid-scale (GS) component and an unresolved subgrid-scale (SGS) component that derives from small-scale eddies. LES has long been recognized as a promising way to predict complex turbulence in engineering applications. Since the success of LES depends strongly on the accurate prediction of the SGS stresses, a number of research groups have discussed several types of SGS model.[1–20] Although the SGS models proposed so far have provided encouraging results, there remain several aspects to be further improved. Among them, an important concern is how to define the filter width used in an SGS model.

In general, we use information of the grid width in representing a filter width (Δ) to evaluate an SGS model. In practical applications, however, the grid widths are largely different in the streamwise and cross-streamwise directions, resulting in grid cells having high aspect ratios. In such a case, we often adopt the cube root of a grid-cell volume for the filter width; i.e., $\Delta = (\Delta x \Delta y \Delta z)^{1/3}$, where Δx, Δy, and Δz are, respectively, the grid widths in the x-, y-, and z-directions of the Cartesian grid system. Although this has been regarded as a standard way to determine the filter width, its superiority over other strategies, such as taking the maximum width in all directions (i.e., $\Delta = \max(\Delta x, \Delta y, \Delta z)$), is not always made clear.

Regarding this issue, Trias *et al.*[21] investigated the definition of the filter width by testing several definitions for decaying homogeneous isotropic turbulence, turbulent channel flow, and flow around a square cylinder. Their results are valuable for understanding how each definition of the filter width performs for these flows, while it remains unclear how the definition of the filter width affects the prediction accuracy in a region far from wall surfaces when using grid cells having high aspect ratios. Such a further detailed investigation is expected to elucidate how we should introduce grid spacing in different directions into the definition of the filter width.

Meanwhile, another approach, referred to as the "implicit LES (ILES)" is becoming increasingly popular in this research field.[22–26] In general, the ILES does not explicitly introduce any SGS model. Instead, the dissipative feature originally included in the discretization scheme is expected for properly extracting the kinetic energy from the GS component. In this sense, the ILES does not always account for the detailed dynamics of small-scale turbulent structures. Furthermore, our previous study[19] elucidated that the prediction accuracy of the ILES suddenly decreases as the grid resolution becomes coarser. This drawback is thought to be related to the aforementioned feature of the ILES, and it is, thus, preferable to introduce an advanced SGS model in obtaining a more grid-independent solution in LES.

Against the above background, the primary objective of the present study is to investigate in detail the effect of the definition of the filter width on the prediction accuracy of an SGS model. For this purpose, we perform *a priori* tests with highly resolved LES data of a backward-facing step (backstep) flow. The reason why we choose a backstep flow is because this flow has strong shear strain as well as massive flow separation behind the step. Although this region is far from wall surfaces, the aspect ratio of a grid cell is generally high owing to the grid topology of a backstep flow.

In general, grid cells with high aspect ratios appear in a region close to a wall surface because we concentrate the grid space selectively in the wall-normal direction. In a near-wall region, however, we do not clearly understand how the definition of the filter width affects the performance of an SGS model. The SGS eddy viscosity originally decreases to zero as a wall approaches, and the effect of narrowing the grid spacing in the wall-normal direction is, thus, included in this general decrease in the SGS eddy viscosity in a near-wall region. Therefore, we cannot sufficiently reveal the effect of a high aspect-ratio grid on the model performance unless the near-wall effect is properly excluded. In this sense, investigating the model performance in the shear layer behind a step enables us to distinguish the effect of the grid aspect ratio from that of near-wall damping.

In this paper, we first report on an unsteady flow simulation for a backstep flow with a sufficiently fine grid. We also calculate the same flow with coarser grid resolutions to confirm the model performance in the simulations. After confirming the basic accuracy of the fine-grid data, we decompose the data into the GS and SGS components for a coarse-grid resolution through grid-filtering using the top-hat filtering operator. We obtain SGS stresses as the reference data by processing the decomposed data. Next, toward the further development of SGS models, we investigate the model performance of several representative SGS models in an *a priori* test using the filtered data. We focus particularly on the model performance in the shear layer downstream of the step so as to elucidate how we should define the filter width on a high aspect-ratio grid for practical LES.

The governing equations and the SGS models investigated in this paper are described in Sec. II, the test case and the computational conditions are summarized in Sec. III, the performance of the SGS models obtained in the *a priori* test is discussed in Sec. IV, and conclusions are given in Sec. V.

II. TURBULENCE MODELS

The canonical governing equations for incompressible turbulence may be written as

$$\frac{\partial \overline{U}_i}{\partial t} + \frac{\partial \overline{U}_i \overline{U}_j}{\partial x_j} = -\frac{1}{\rho}\frac{\partial \overline{P}}{\partial x_i} + \frac{\partial}{\partial x_j}\left(2\nu S_{ij} - \tau_{ij}{}^a\right),$$
$$\frac{\partial \overline{U}_i}{\partial x_i} = 0, \quad S_{ij} = \frac{1}{2}\left(\frac{\partial \overline{U}_i}{\partial x_j} + \frac{\partial \overline{U}_j}{\partial x_i}\right), \tag{1}$$

where $\overline{(\ )}$ denotes a filtered value. The quantities ρ, $\overline{P}$, $\overline{U}_i$, ν, and S_{ij} are the density, filtered static pressure, filtered velocity, kinematic viscosity, and strain-rate tensor, respectively. Note that $\tau_{ij}{}^a$ is defined as $\tau_{ij} - \tau_{kk}\delta_{ij}/3$, where the SGS stress τ_{ij} is originally expressed as

$$\tau_{ij} = \overline{U_i U_j} - \overline{U}_i \overline{U}_j. \tag{2}$$

Therefore, $\overline{P}$ in Eq. (1) includes $\rho\tau_{kk}/3$ in this paper.

The following sections briefly describe the SGS models investigated in this work.

A. Conventional linear eddy-viscosity model

First, to investigate the characteristics of conventional SGS frameworks, two eddy-viscosity models (EVMs) were tested: the Smagorinsky model[1] (SM, hereinafter) and the dynamic Smagorinsky model[4,5] (DSM, hereinafter). The canonical form of a linear EVM is

$$\tau_{ij}{}^a = -2\,\nu_{SGS}\,S_{ij}, \tag{3}$$

where ν_{SGS} is the SGS eddy viscosity. In the SM, ν_{SGS} is modeled as

$$\nu_{SGS} = (C_S f_S \Delta)^2 \sqrt{2S^2}, \quad f_S = 1 - \exp\left(-\frac{y^+}{A}\right), \tag{4}$$

where $y^+ = u_\tau y/\nu$ (u_τ: friction velocity) and $S^2 = S_{ij}S_{ij}$. In Eq. (4), $C_S = 0.1$ and $A = 25$ are generally used constants. In this model, the filter width is generally defined as $\Delta = (\Delta x \Delta y \Delta z)^{1/3}$ in the Cartesian grid system.

In contrast, ν_{SGS} in the DSM is

$$\nu_{SGS} = C\Delta^2 \sqrt{2S^2}, \tag{5}$$

where the coefficient C is locally determined using the dynamic procedure proposed by Germano *et al.*[4] together with the least squares approximation of Lilly.[5] In fact, the coefficient is calculated as $(C\Delta^2)$, once the filter-width ratio between the test and grid filters is determined.

B. Conventional scale-similarity model

Although introducing a linear EVM into existing computational fluid dynamics (CFD) codes is straightforward, a crucial problem is that its principal direction does not align with the real SGS-stress tensor. Alternatively, the concept of a "scale-similarity model" is worth noting. A representative scale-similarity model was proposed by Bardina *et al.*[2] as

$$\left(\overline{U}_i - \overline{\overline{U}}_i\right)\left(\overline{U}_j - \overline{\overline{U}}_j\right). \tag{6}$$

According to this modeling concept, we introduce the following Bardina-type SGS model (BRD, hereinafter):

$$\tau_{ij}{}^a = C_B \left\{\left(\overline{U}_i - \widehat{\overline{U}}_i\right)\left(\overline{U}_j - \widehat{\overline{U}}_j\right)\right\}^a, \tag{7}$$

where C_B is the model constant and $\widehat{(\ )}$ denotes a test-filtered value. Note that we used top-hat filter to calculate $\widehat{(\ )}$ in this work. The SGS turbulence energy k_{SGS} may be evaluated as

$$k_{SGS} = \frac{1}{2}\tau_{kk} = \frac{C_B}{2}\left(\overline{U}_k - \widehat{\overline{U}}_k\right)\left(\overline{U}_k - \widehat{\overline{U}}_k\right). \tag{8}$$

We specify the model constant $C_B = 2$ with the test-filter width being twice the grid width.

Meanwhile, another type of SGS model based on the modified Leonard stress[3] is considered,

$$\overline{\overline{U}_i\overline{U}_j} - \overline{\overline{U}}_i\overline{\overline{U}}_j. \tag{9}$$

Similarly to the use of the Bardina model, the following model (mLND, hereinafter) can be used:

$$\tau_{ij}{}^a = C_L\left(\widehat{\overline{U}_i\overline{U}_j} - \widehat{\overline{U}}_i\widehat{\overline{U}}_j\right)^a, \tag{10}$$

where C_L is the model constant and k_{SGS} may be evaluated as

$$k_{SGS} = \frac{1}{2}\tau_{kk} = \frac{C_L}{2}\left(\widehat{\overline{U}_k\overline{U}_k} - \widehat{\overline{U}}_k\widehat{\overline{U}}_k\right). \tag{11}$$

We specify the model constant $C_L = 0.5$ with the test-filter width being twice the grid width.

It is noted that the model constants presently used (i.e., $C_B = 2$ and $C_L = 0.5$) were determined only to successfully predict a reasonable level of the SGS values. Therefore, further detailed discussion on the model constants is necessary, although the results given below are sufficient for understanding essential features of the models.

C. Stabilized mixed model

We investigate an anisotropic one-equation SGS model proposed by Abe.[14] This model is constructed by combining an EVM with an extra anisotropic term (EAT). The SGS stress is modeled as

$$\tau_{ij}{}^a = -2\nu_{SGS}S_{ij} + 2k_{SGS}b_{ij}^{EAT}. \tag{12}$$

The anisotropy tensor b_{ij}^{EAT} in Eq. (12) is modeled as

$$b_{ij}^{EAT} = \frac{\tau'_{ij} - (-2\nu'S_{ij})}{\tau'_{kk} - (-2\nu'S_{kk})} - \frac{1}{3}\delta_{ij}, \quad \nu' = -\frac{\tau'_{ij}{}^aS_{ij}}{2S^2},$$
$$\tau'_{ij} = \left(\overline{U}_i - \widehat{\overline{U}}_i\right)\left(\overline{U}_j - \widehat{\overline{U}}_j\right), \tag{13}$$

where $\tau'_{ij}{}^a = \tau'_{ij} - \tau'_{kk}\delta_{ij}/3$. In Eq. (13), ν' is an equivalent eddy viscosity obtained using an EVM-type linear approximation for τ'_{ij}, which is given by the BRD with $C_B = 1$.

Concerning the linear EVM in Eq. (12), this model adopts the SGS model proposed by Inagaki[13] with some minor modifications. The SGS eddy viscosity is modeled as

$$\nu_{SGS} = C_{SGS}f_{SGS}\sqrt{k_{SGS}}\,\Delta, \quad f_{SGS} = 1 - \exp\left\{-\left(\frac{y'_\varepsilon}{A_0}\right)^{4/3}\right\},$$
$$y'_\varepsilon = \left(\frac{u_\varepsilon y}{\nu}\right)\sqrt{C_l\frac{y}{\Delta}}, \quad u_\varepsilon = (\nu\varepsilon_{SGS})^{1/4}, \tag{14}$$

where the filter width is defined as $\Delta = \sqrt{\max(\Delta x\Delta y, \Delta y\Delta z, \Delta z\Delta x)}$, which is different from the original filter width (i.e.,

$\Delta = (\Delta x\Delta y\Delta z)^{1/3}$). Note that the filter-width definition used in this model is the same as the maximum width in all directions (i.e., $\Delta = \max(\Delta x, \Delta y, \Delta z)$) under the condition that $\Delta x = \Delta z \gg \Delta y$.

In this work, k_{SGS} and ε_{SGS} are evaluated using the equations as

$$\frac{Dk_{SGS}}{Dt} = \frac{\partial}{\partial x_j}\left\{\left(\nu + \frac{\nu_{SGS}}{\sigma_k}\right)\frac{\partial k_{SGS}}{\partial x_j}\right\} - \tau_{ij}\frac{\partial \overline{U}_i}{\partial x_j} - \varepsilon_{SGS},$$
$$\varepsilon_{SGS} = C_\varepsilon\frac{k_{SGS}^{3/2}}{\Delta} + \frac{2\nu k_{SGS}}{y^2}. \tag{15}$$

The model constants are

$$C_{SGS} = 0.05, \quad A_0 = 30, \quad C_l = 4, \quad C_\varepsilon = 0.835, \quad \sigma_k = 0.5. \tag{16}$$

More detailed descriptions are given in Abe.[14,15]

Considering that the EAT in Eq. (12) yields no undesirable extra energy transfer between the GS and SGS components, we expect this anisotropic SGS model to successfully predict the SGS-stress anisotropy with no appreciable effect on the computational stability. In this sense, this SGS model is regarded as a combination of a linear EVM and a scale-similarity model effectively modified for stable computation and it is, thus, referred to as the "stabilized mixed model" (SMM, hereinafter).

III. TEST CASE AND COMPUTATIONAL CONDITIONS

We deal with a backstep flow that corresponds to the experiment of Kasagi and Matsunaga.[27] A schematic view and the grid systems used are shown in Fig. 1. The presence of massive separation downstream of the step allows an SGS model to be investigated under conditions representative of complex separated flows. The origin of coordinates is located at the step corner, and we specify x as the streamwise, y as the wall-normal, and z as the spanwise directions, respectively. The present backstep flow consists of the upstream section with a duct height of $2H$ and the downstream section with a duct height of $3H(= 2H + H)$, where H is the step height, resulting in an expansion ratio of $3H/2H = 1.5$. Note that the driver section in Fig. 1(a) is introduced to provide fully developed channel-flow data to the inlet of the upstream section, corresponding to the experimental condition.[27]

Three grid resolutions are selected as shown in Figs. 1(b)–1(d). The grid resolution is basically controlled by varying the grid numbers with the domain size being fixed. The domain size in the spanwise (z) direction is set at $3.2H$, and the resultant grid resolutions in this direction are $\Delta z = 0.025H$ (fine), $0.05H$ (medium), and $0.1H$ (coarse), respectively. A notable feature of the present simulations is that the grid spacing in the streamwise (x) direction is the same as that in the z-direction for computational domains with which we are mainly concerned, i.e., the driver section, the upstream section ($-3 < x/H < 0$), and the downstream section from $x/H = 0$ to $x/H = 12$ that sufficiently includes a separation bubble.

We intentionally adopts uniform grid spacing in the x-direction even around the step ($x/H = 0$), although we generally concentrate grid nodes there for this kind of flow fields. This is because we want to conduct an *a priori* test of SGS models using the computational results for the fine-grid case. Once we successfully obtain high-quality flow data for the fine-grid resolution in Fig. 1(b), we can introduce a strategy similar to our previous study[19] in which we obtain reduced data for coarser grid resolutions by filtering the fine-grid data in the x- and
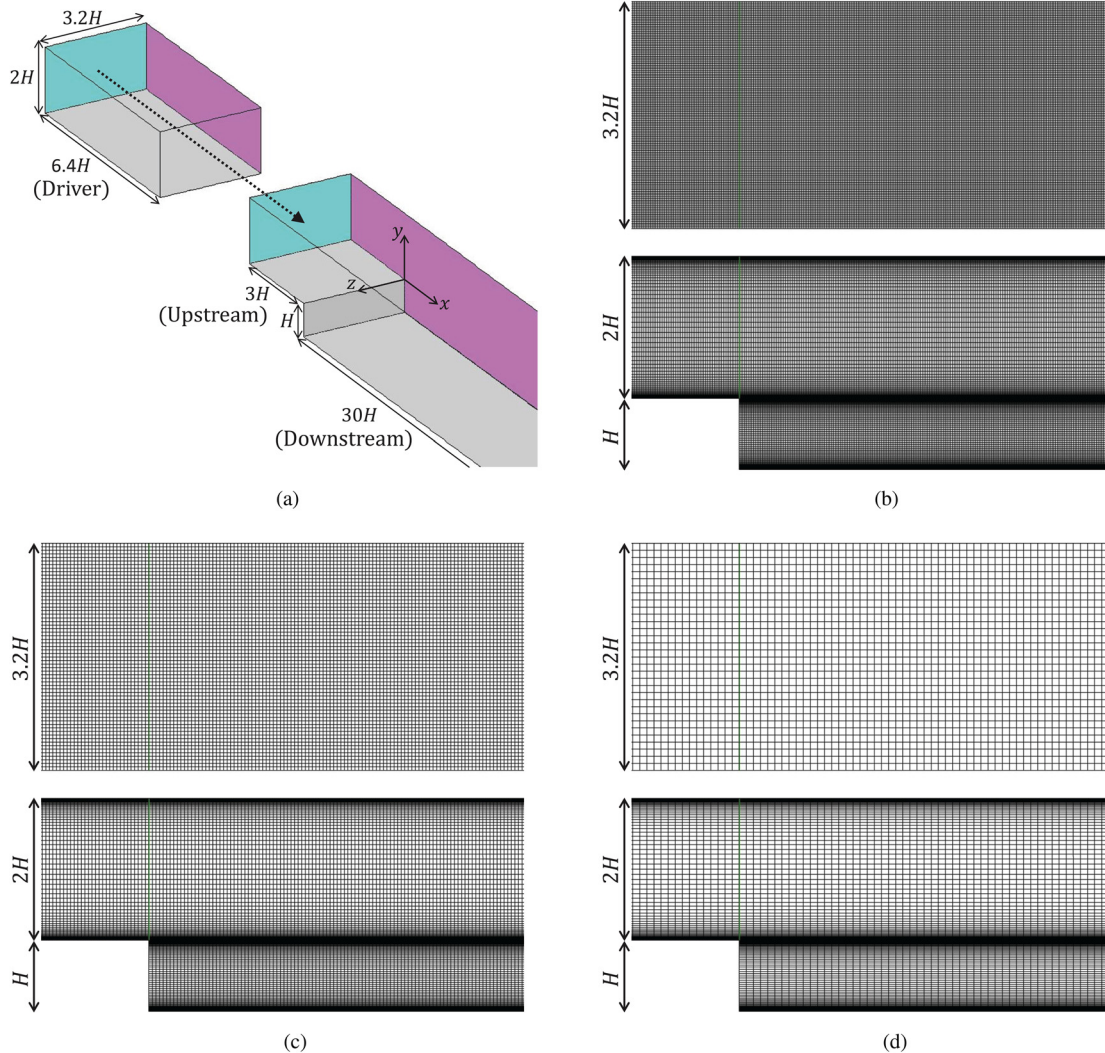
FIG. 1. Schematic view of the backstep flow and grid resolutions tested in this work: (a) a schematic view, (b) fine grid ($\Delta x = \Delta z = 0.025$), (c) medium grid ($\Delta x = \Delta z = 0.05$), and (d) coarse grid ($\Delta x = \Delta z = 0.1$). Note that number of grid nodes in the y-direction is fixed for all test cases. Figures (b)–(d) partially show the computational domain around the step corner from $x/H \sim -1.5$ to $x/H \sim 5.5$.

z-directions. The uniform grid spacing in a direction means that the filter width in the direction is also the same at any grid point. Therefore, such a uniform grid spacing enables us to investigate properly how an SGS model locally works. Note that we use the same grid number and spacing in the y-direction for all three cases, and the filtering is thus not operated in the y-direction in this study. Comparing the results in an *a priori* test with the corresponding filtered data enables us to investigate in detail the essential feature of an SGS model.

The computational conditions are summarized in Table I. We fix the flow Reynolds number in the driver channel at $Re_\tau = u_\tau H/\nu = 290$ based on the friction velocity and the half-duct height that is the same as the step height H (Fig. 1). This condition was taken from the experiment of Kasagi and Matsunaga.[27] The resultant bulk Reynolds number $Re_H = U_b H/\nu$ for all test cases is also included in Table I, where U_b is the mean velocity at the center of the driver

channel. Kasagi and Matsunaga[27] reported $Re_H \sim 5500$ in their work, and, we, thus, find that the values of Re_H obtained from the present simulations are in reasonable agreement with the experimental value. In this study, we reduced the number of grid nodes in the x- and z-directions, in half from the BSF (fine-grid case) to the BSM (medium-grid case) and in quarter from the BSF to the BSC (coarse-grid case), respectively, except for the far-downstream region of $x/H > 12$. Because a uniform grid spacing is adopted in the x-direction, the grid resolution near the step appears a little too coarse for LES. Therefore, the present computational condition is much more tough for an SGS model relative to the general computational condition in which grid nodes tend to be concentrated in the x-direction close to the step.

In the real unsteady calculations listed in Table I, we use the anisotropy-resolving hybrid LES/RANS (Reynolds-Averaged Navier–Stokes) (HLR) model proposed by Abe[28] (HLR model, hereinafter). This HLR model adopts

TABLE I. Computational conditions for the backstep flow. The Reynolds number for the driver channel flow is fixed at $Re_\tau = u_\tau H/\nu = 290$ taken from the corresponding experiment.[27]

Case	Grid type	Driver domain	Grid numbers	$\Delta x/H$	$\Delta y/H$	$\Delta z/H$	Δx^+	Δy^+	Δz^+
BSF	Fine	6.4 H × 2 H × 3.2 H	257 × 81 × 129	0.025	1×10^{-3}–0.07	0.025	7.25	0.29–20	7.25
BSM	Medium	6.4 H × 2 H × 3.2 H	129 × 81 × 65	0.05	1×10^{-3}–0.07	0.05	14.5	0.29–20	14.5
BSC	Coarse	6.4 H × 2 H × 3.2 H	65 × 81 × 33	0.1	1×10^{-3}–0.07	0.1	29	0.29–20	29

Case	Grid type	Upstream domain	Grid numbers	$\Delta x/H$	$\Delta y/H$	$\Delta z/H$	Δt^+	Re_H
BSF	Fine	3 H × 2 H × 3.2 H	121 × 81 × 129	0.025	1×10^{-3}–0.07	0.025	2×10^{-4}	5719
BSM	Medium	3 H × 2 H × 3.2 H	61 × 81 × 65	0.05	1×10^{-3}–0.07	0.05	2×10^{-4}	5709
BSC	Coarse	3 H × 2 H × 3.2 H	31 × 81 × 33	0.1	1×10^{-3}–0.07	0.1	2×10^{-4}	5694

Case	Grid type	Downstream domain	Grid numbers	$\Delta x/H (x/H < 12)$	$\Delta x/H (12 < x/H < 30)$	$\Delta y/H$	$\Delta z/H$
BSF	Fine	30 H × 3 H × 3.2 H	601 × 161 × 129	0.025	0.025–0.25	1×10^{-3}–0.07	0.025
BSM	Medium	30 H × 3 H × 3.2 H	341 × 161 × 65	0.05	0.05–0.25	1×10^{-3}–0.07	0.05
BSC	Coarse	30 H × 3 H × 3.2 H	211 × 161 × 33	0.1	0.1–0.25	1×10^{-3}–0.07	0.1

the aforementioned SMM in the LES region, while a one-equation nonlinear eddy-viscosity model is used in the RANS region. A notable feature of this HLR model is in automatically guaranteeing a full LES under the condition of a sufficiently fine grid resolution. In fact, for the fine-grid (BSF) and medium-grid (BSM) cases in Table I, the distribution of the LES/RANS switching function indicates the "LES" in the computational domain with which we are mainly concerned ($x/H < 12$). Even in the coarse-grid case (BFC), the distribution indicates almost the "LES" except for a limited region close to the upper wall. Therefore, the computational results are nearly obtained by LES using the SMM. A further description about this HLR model is given in Appendix A.

The computational procedure adopted in this work is the same as that of Abe.[28] This procedure is an unstructured finite-volume procedure nearly identical to that of Muto *et al.*,[29] where a vertex-centered type of storage is used on a grid. Although the second-order central difference scheme is basically applied to discretize the spatial derivatives, the convection terms of the momentum equations are discretized adopting a blending scheme of the second-order central difference (98%) and the first-order upwind scheme (2%) so as to eliminate unnecessary numerical instability that may appear close to the step. It is also noted that the convection term of the turbulence energy is discretized by the second-order upwind scheme. The time marching is based on the fractional step method,[30] in which the second-order Crank-Nicolson scheme is used for the velocity equations whereas the first-order Euler implicit scheme is used for the transport equation of k_{SGS}. The coupling of the velocity and pressure fields is based on the simplified marker and cell method.[31] The flow rate on the control-volume surface is estimated using the Rhie–Chow interpolation.[32] In previous studies, we investigated the effects of the blending scheme used for the momentum equation,[33] as well as the first-order time-marching scheme and the second-order upwind scheme adopted for the k_{SGS}-transport equation.[14,15] These investigations confirmed that the time-integration and space-discretization schemes used in these transport equations had no important effect on the final conclusions. Concerning the wall distance used in the present calculations, we introduce the method of Inagaki,[13] which reasonably provides the distribution of wall distance for complex geometries.

For the boundary conditions, the periodic condition is imposed in the spanwise (z) direction, whereas the no-slip conditions are specified at the wall surfaces. The Reynolds number in the present test case is not high, and we can, thus, conduct wall-resolved simulations using the grid resolutions given in Table I. In the driver channel, the periodic condition is also imposed in the streamwise (x) direction with a constant streamwise pressure gradient. At the inlet of the upstream section, instantaneous flow distributions obtained by the driver-channel calculation are imposed at each time step so as to mimic a fully developed inlet condition. At the outlet boundary, zero streamwise gradients are prescribed.

IV. RESULTS AND DISCUSSION

A. Basic performance of the present simulations

First, instantaneous vortex structures for three grid-resolution cases in Table I are shown in Fig. 2, where they are visualized using the second invariant of the velocity-gradient tensor ($Q = -(1/2)(\partial \overline{U}_i/\partial x_j)(\partial \overline{U}_j/\partial x_i)$). We can recognize many vortices in the upstream section as well as in the shear-layer region at $y/H \sim 0$ downstream of the step. This means that the inlet boundary condition using a driver section works sufficiently well to specify instantaneous distributions of a fully developed channel flow. It is also found that the visualized vortex structures decrease as the grid resolution becomes coarse.
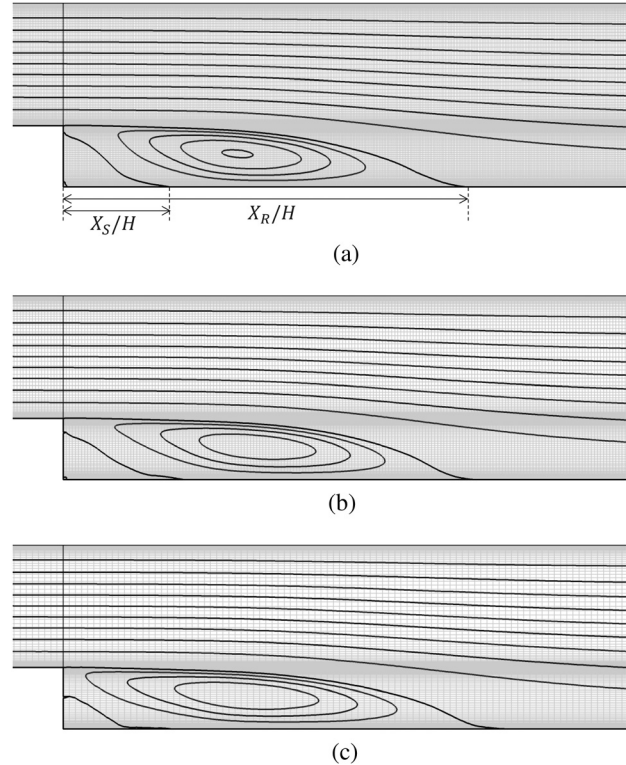
Figure 3 compares the streamlines obtained from the mean-velocity distributions for three grid-resolution cases. Note that all statistics in this work are ensemble-averaged in the spanwise (z) direction as well as in time. In all cases, not only a large separation bubble but also a secondary small separation near the step are successfully predicted, although the separation bubble predicted in the BSC looks a little longer than the other two cases. To allow a more detailed discussion, the reattachment length (X_R/H) and the secondary separation point (X_S/H) are compared with those of the experiment[27] in Table II. The predictions of the BSF are in fairly good agreement with the experimental data. Additionally, the results of the BSM are generally in good agreement with the experimental data, although there are slight overpredictions. The results of the BSC generally agree with the experimental data, but the predicted separation bubble is longer than
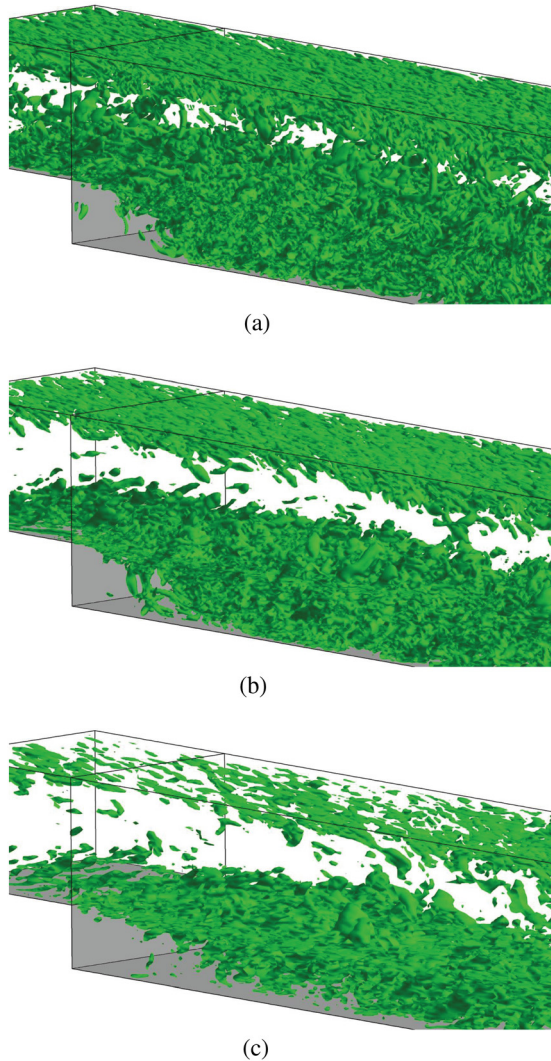
FIG. 2. Comparison of the vortex structures visualized using the second invariant of the velocity-gradient tensor (where the criterion is $Q^+ = 0.6$, normalized by the wall parameters in the driver channel): (a) BSF, (b) BSM, and (c) BSC.

FIG. 3. Comparison of streamlines: (a) BSF, (b) BSM, and (c) BSC.

that in the experiment. In this work, we intentionally adopt a uniform grid spacing in the x-direction even near the step so as to properly conduct an *a priori* test of SGS models in later sections. The streamwise grid resolution for the BSC is $\Delta x = 0.1H$, meaning that there are only 10 grid nodes per the step-height width, resulting in a high aspect ratio of $\Delta x/\Delta y \sim 100$. Considering such a tough condition, it is considered that the present model generally works well even for the BSC, although there remains a room to be further improved in its performance. Note that to discuss the necessity of an SGS model for coarse grid resolutions, another calculation for the BSC with no SGS model (i.e., the ILES) is performed for comparison. The results and discussion are presented in Appendix B.

Next, to confirm the basic features of the present simulations in more detail, we obtain the turbulence statistics from the computational

results. Figure 4 compares the distributions of the mean velocity, turbulence energy, and Reynolds-shear (Re-shear) stress for three grid-resolution cases with those of the experiment.[27] Note that the results of the turbulence energy and the Re-shear stress consist of both GS and SGS components (GS+SGS: "total," hereinafter). As seen in the figures, we select five streamwise positions for comparison, i.e., $x/H = 1, 3, 5, 7$, and 9. The figures show that the predictions are generally in good agreement with the experimental data for all grid resolutions, although we see some overpredictions particularly in the separated region. Even for the BSC, the predicted turbulence statistics generally correspond to the experimental data, and it is, thus, considered that their slight discrepancies may finally affect the prediction of X_R/H in Table II.

B. Comparison of the decomposed filtered SGS data with the computational results

As shown in the Sec. IV A, we confirm the good agreement of the results for the fine-grid case (BSF) with the experimental data. This

TABLE II. Comparison of the reattachment length (X_R/H) and the secondary separation point (X_S/H).

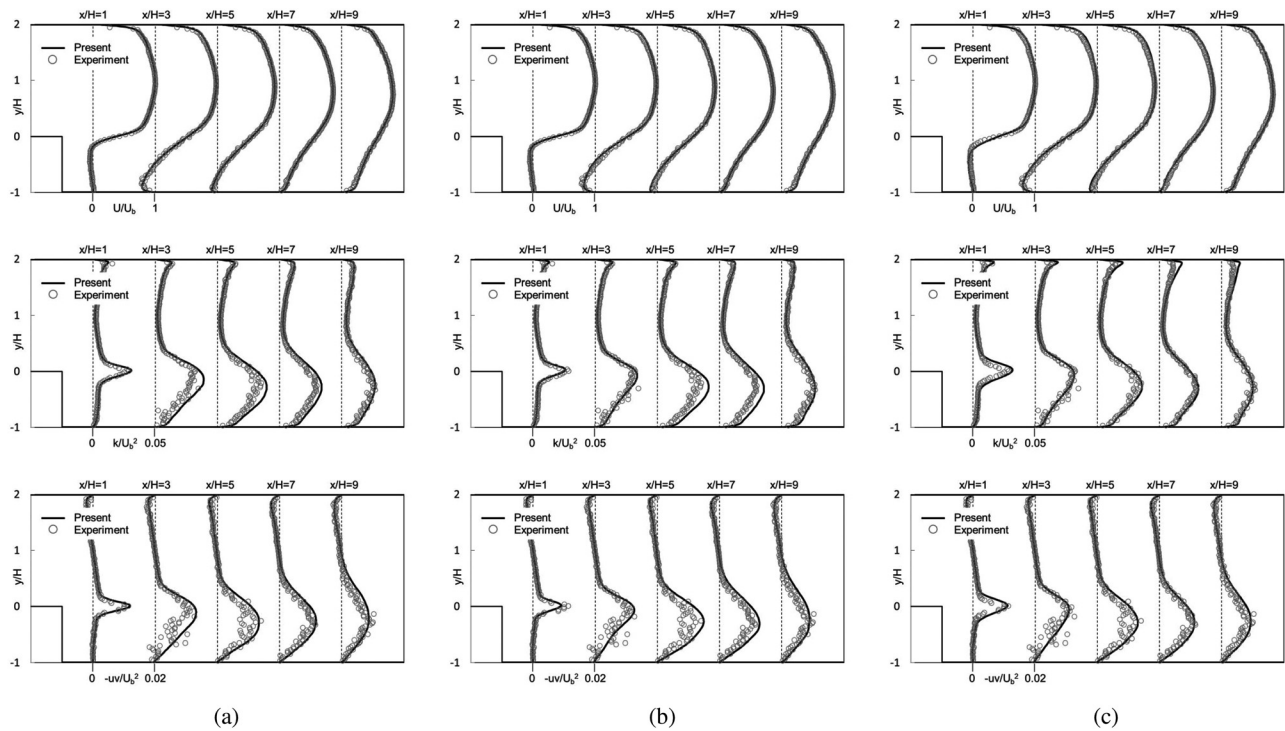| Case	Exp.[27]	BSF	BSM	BSC
X_R/H	6.51	6.54 (+0.5%)	6.67 (+2.5%)	7.19 (+10.4%)
X_S/H	1.70	1.72	1.95	1.75

FIG. 4. Computational results of the mean velocity, total (GS+SGS) turbulence energy, and total Re-shear stress: (a) BSF, (b) BSM, and (c) BSC. Note that each scale specified on the horizontal axis in the figure is applicable at all x/H locations.

suggests that we can conduct an *a priori* test of SGS models using these BSF data. For this purpose, we generate filtered data for the coarse-grid resolution of the BSC from the BSF data. First, to check how the SGS model affects the total turbulence statistics in the BSF, Fig. 5 compares the SGS turbulence energy and the SGS Re-shear stress with the experimental data. Note that the SGS turbulence energy is directly obtained using its transport equation, Eq. (15), whereas the SGS Re-shear stress is calculated algebraically using Eq. (12) with $i=1$ and $j=2$. It is readily seen that the SGS components in the BSF are very small compared with the corresponding turbulence statistics, and therefore, the statistics in the BSF are almost covered by the GS components. This indicates that we can sufficiently perform an *a priori* test by using the filtered values obtained from the GS components of the BSF data.

Our next concern is the quality of the filtered data because we have to generate these data from instantaneous flow-field data. In our previous study,[19] we applied the filtering operator in the x- and z-directions, both of which are homogeneous directions in a fully developed channel flow. For a backstep flow, however, the homogeneous direction is only the z-direction, and the number of sample data is, thus, 128 even in the BSF at an instantaneous time step. Therefore, as a remedy, we apply 20 instantaneous snapshot data for calculating an ensemble-averaged value. Figure 6 compares the turbulence statistics obtained from the above snapshot data with those of the long-time average for the BSF. The snapshot data show no significant conflict with the long-time averaged data, although statistical convergence is not perfect and some wavy profiles remain in the Re-shear stress in
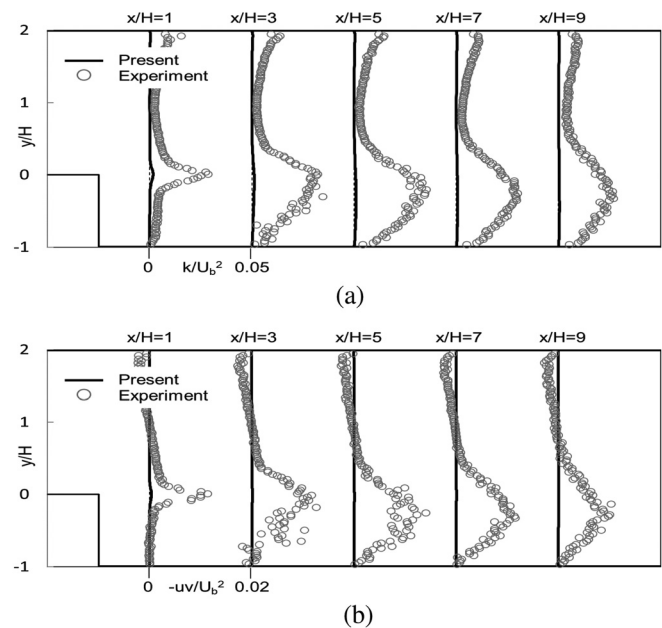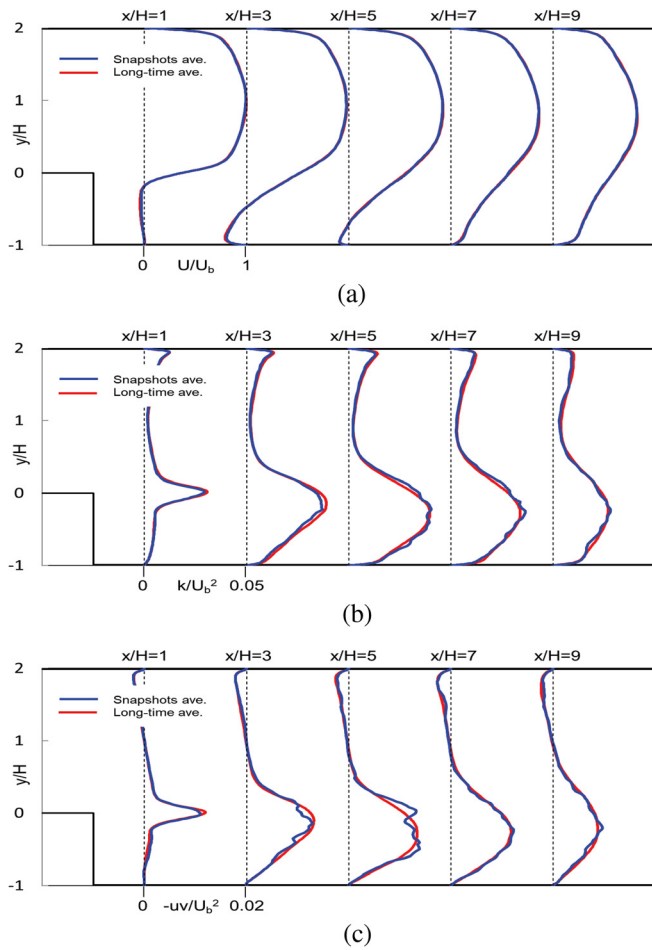

FIG. 5. Comparison of the SGS components in the fine-grid case (BSF) with the corresponding experimental data: (a) SGS turbulence energy and (b) SGS Re-shear stress.

FIG. 6. Comparison of statistics obtained from 20 snapshot data with those of the long-time average (BSF): (a) mean velocity, (b) turbulence energy, and (c) Re-shear stress. Note that the snapshot-averaged data are only composed of the GS component. All data are ensemble averaged in the spanwise (z) direction and time.

Fig. 6(c). The fact that the effects of the SGS stress are intentionally excluded from the snapshot data confirms that the statistical distributions are sufficiently reproduced only by the GS data for the BSF.

We then decompose the BSF data into the GS and SGS components for the coarse-grid (BSC) resolution through grid-filtering using the top-hat filtering operator. To obtain the filtered data, we apply the filtering operation in the x- and z-directions, adopting the same grid spacing given in Table I. We regarded these decomposed data as the "reference data" for the corresponding coarse grid resolution. Note that we evaluated the SGS stresses in the reference data using the original definition in Eq. (2).

Here, a concern may emerge about how the filtering operator in the y-direction affects the evaluation of the SGS stresses. Addressing this issue, we investigate SGS values calculated using two- and three-dimensional filtering operations in Appendix C. We, thus, find that the filtering operator in the x- and z-directions successfully captures fundamental features of SGS components, and the filtering operator in the y-direction does not largely affect the SGS values, at least in the

shear-layer region that is the primary concern in this work. This also confirms that the filtering operation with a narrow grid width does not suppress SGS values.

Figure 7 compares the BSC results of the real calculation with the reference data. Both the SGS turbulence energy and SGS Re-shear stress generally correspond well to the reference data, although some overpredictions are seen at $x/H = 1$.

Meanwhile, Fig. 8 shows a little different aspect between the instantaneous distribution of k_{SGS} for the BSC and that of the reference data. Although the level of k_{SGS} in the real calculation generally corresponds to that of the reference data, its distribution looks a little too diffusive. This difference needs to be discussed in more detail for further improvement of the model performance.

C. *A priori* test of several SGS models

This section reports on an *a priori* test of several SGS models. For this purpose, we calculate the SGS eddy viscosity ν_{SGS} for each SGS model using the decomposed filtered data, and the distributions are compared with those of the reference data. To obtain ν_{SGS} as the reference data, we introduce a method similar to Eq. (13): An equivalent SGS eddy viscosity is calculated as follows:

$$\nu_{SGS} = -\frac{\tau_{ij}{}^a S_{ij}}{2S^2}, \quad (17)$$

where τ_{ij} is the aforementioned reference SGS stresses obtained from the filtered data. Note that an EVM-type SGS model introducing this equivalent ν_{SGS} into Eq. (3) perfectly reproduces the energy transfer between the GS and SGS components as the original τ_{ij} does, including both the forward and backward scatters.

We investigate five SGS models, namely, the SM, DSM, BRD, mLND, and SMM. Among them, ν_{SGS} is calculated for the BRD and
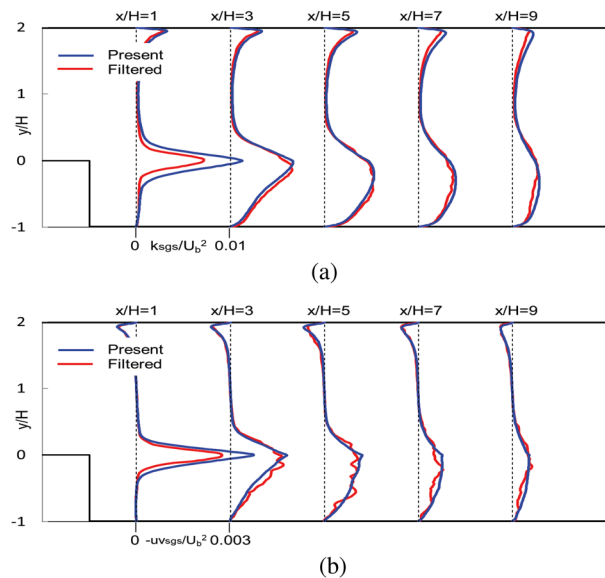
FIG. 7. Comparison of the results for the BSC in the real calculation with the reference data obtained from the BSF results through the grid-filtering process: (a) SGS turbulence energy and (b) SGS Re-shear stress.
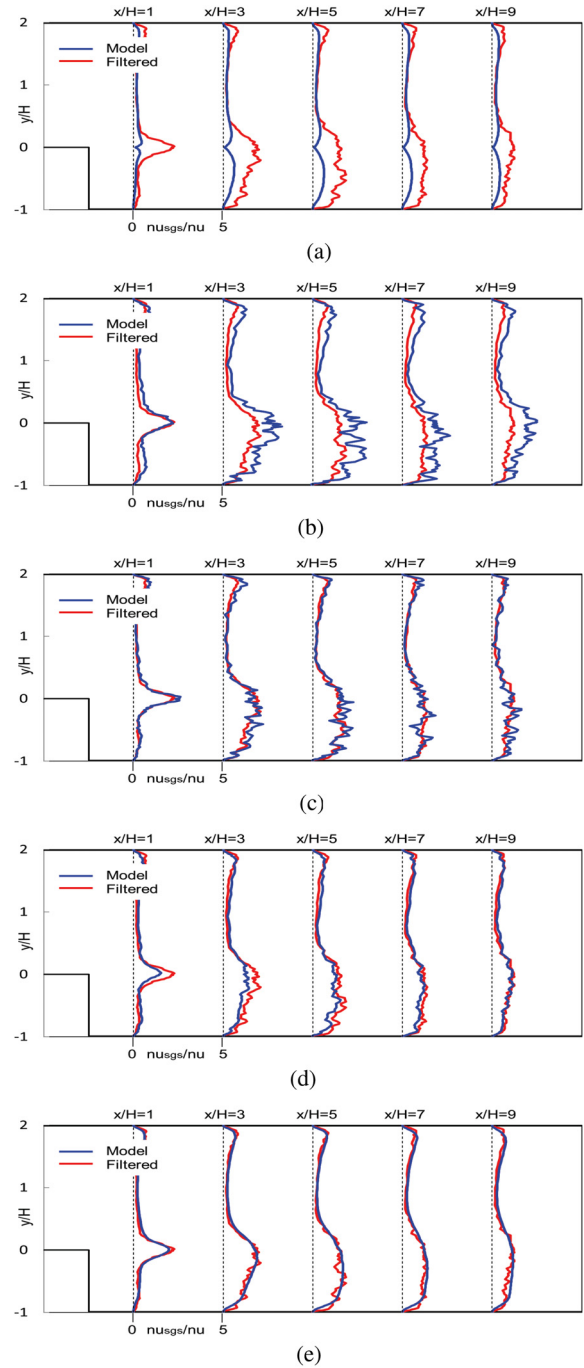
(a)

(b)
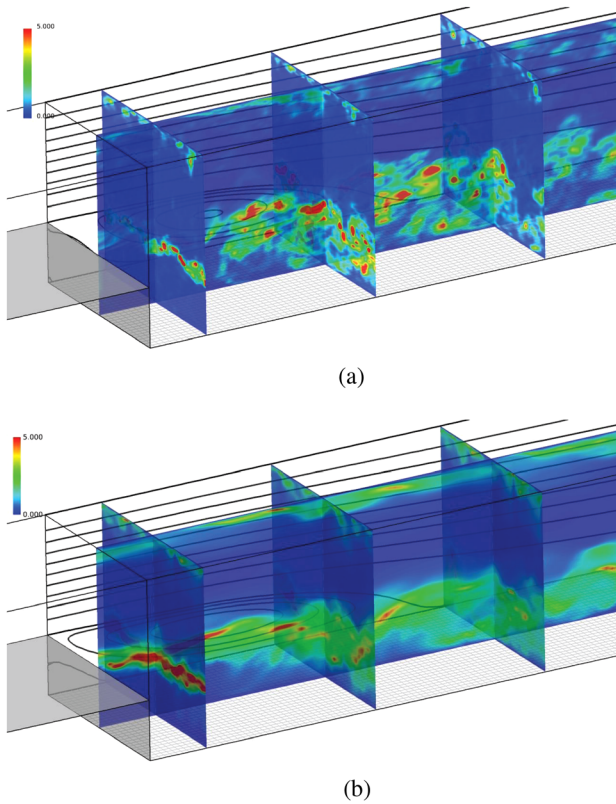
FIG. 8. Comparison of the instantaneous distributions of the SGS turbulence energy for the BSC in the real calculation with filtered data obtained from the BSF results (where the color range is 0 (blue) < k_{SGS}^+ < 5 (red), normalized by the wall parameters in the driver channel): (a) filtered data obtained from the BSF results and (b) real calculation (BFC).

(a)

(b)

(c)

(d)

(e)

FIG. 9. Comparison of the SGS eddy-viscosity distributions evaluated in an *a priori* test with the reference data obtained from the filtered values: (a) SM, (b) DSM, (c) BRD, (d) mLND, and (e) SMM.

mLND by applying Eqs. (7) and (10), respectively, to Eq. (17). The other models (i.e., the SM, DSM, and SMM) evaluate ν_{SGS} according to Eqs. (4), (5), and (14), respectively. Note that k_{SGS} used in the SMM is calculated using $\tau_{kk}/2$ obtained from the filtered data.

Figure 9 compares the distributions of ν_{SGS} obtained in an *a priori* test with the reference data. An important feature as seen in Fig. 9(a) is that ν_{SGS} for the SM is much smaller than the reference data. Particularly in the shear-layer region at $y/H \sim 0$, ν_{SGS} is clearly suppressed by the extremely narrow grid width in the y-direction. We, therefore, question whether the cube root of the grid-cell volume (i.e., $\Delta = (\Delta x \Delta y \Delta z)^{1/3}$) is indeed suitable for the filter-width definition under the condition of such a high aspect-ratio grid.

In contrast, the DSM returns generally reasonable prediction for ν_{SGS}, although some overestimation is seen in the downstream region. As previously mentioned, the coefficient in the DSM is calculated as $(C\Delta^2)$ at once, and the DSM, thus, does not depend explicitly on the filter-width definition. As for scale-similarity models, both the BRD and the mLND generally provide predictions that are in good agreement with the reference data. In the case of the SMM, the predicted ν_{SGS} also corresponds well to that of the reference data, despite the fact that ν_{SGS} in this model has the general algebraic formulation of the

one-equation SGS model. Considering the fact that the SMM adopts a different type of filter-width definition, an idea emerges that this may cause such a difference as seen in the model performance between the SM and the SMM. This is important knowledge obtained in the

present work, and more detailed discussion is needed for further development of an SGS model.

D. Effect of a filter-width definition on the model performance

On the basis of the aforementioned discussion, we investigate the effect of the filter-width definition on the model performance for grid cells having high aspect ratios. We, thus, calculate ν_{SGS} for the SMM and SM using another definition of Δ. In this section, the cube root of a grid-cell volume (i.e., $\Delta = (\Delta x \Delta y \Delta z)^{1/3}$ is used for the SMM (mSMM, hereinafter) whereas the maximum width in all directions (i.e., $\Delta = \max(\Delta x, \Delta y, \Delta z)$) is used for the SM (mSM, hereinafter).

Figure 10 compares ν_{SGS} evaluated in an *a priori* test with the reference data. As seen in Fig. 10(a), the mSMM returns a value of ν_{SGS} that is much smaller than that returned by the original SMM. Particularly, in the shear-layer region at $y/H \sim 0$, ν_{SGS} is clearly suppressed by an extremely narrow grid width in the y-direction. Considering that such a difference between the prediction and reference data is already shown in Fig. 9(a) for the original SM, it is considered that the cube root of a grid-cell volume is likely to cause a considerable suppression in predicting ν_{SGS} for grid cells with high aspect ratios.

Meanwhile, it is a little surprising that ν_{SGS} of the mSM has a reasonable distribution even in the shear layer. This distribution shows an aspect similar to that of the original SMM that adopts the same filter-width definition under $\Delta x = \Delta z$. It is then suggested that an alternative option for the filter width (e.g., $\Delta = \max(\Delta x, \Delta y, \Delta z)$) may be better for predicting ν_{SGS} in LES for complex turbulence, including grid cells with high aspect ratios.

To confirm the effect of the filter-width definition in a real simulation, we conduct an *a posteriori* test for the BSC using the mSMM
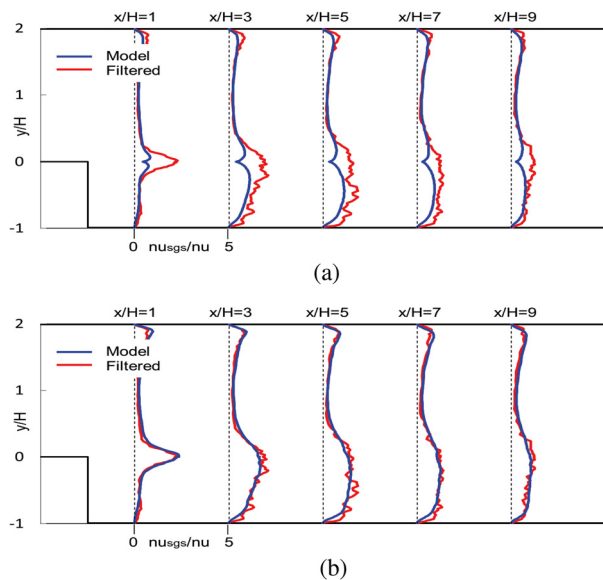
(BSCmSMM, hereinafter). Figure 11 shows the streamlines, SGS turbulence energy, and SGS *Re*-shear stress, whereas Table III compares the reattachment length (X_R/H) and the secondary separation point (X_S/H). Although the streamlines of the BSCmSMM generally look reasonable, a slightly longer separation bubble is obtained compared with that of the original BSC. Furthermore, we see a considerable suppression of the SGS values in the shear-layer region. Further modification of the model constants may improve the fundamental prediction accuracy to some extent because this calculation is performed by simply redefining the filter width. However, it is considered that the suppression of the SGS values in the shear-layer region does not disappear even if further tuning is performed. We, thus, conclude that this is an essential feature of SGS models using the cube root of a grid-cell volume.

E. Investigation of algebraic models for the SGS turbulence energy

As previously discussed, the SMM generally works well in predicting complex turbulence under low grid-resolution conditions. This model is however a one-equation SGS model, and we, thus, have to solve the transport equation of k_{SGS} in Eq. (15) to obtain its distribution. To avoid this operation, Inagaki and Kobayashi[34] recently investigated the possibility of excluding the k_{SGS}-transport equation by
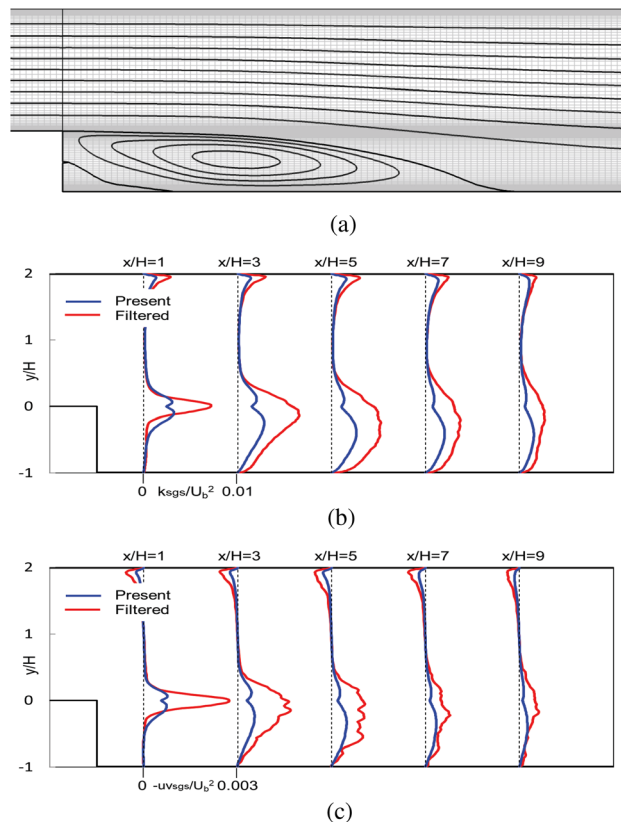

(a)

(b)

(c)

FIG. 11. Computational results of the real calculation for the BSC using the mSMM: (a) streamlines, (b) SGS turbulence energy, and (c) SGS *Re*-shear stress.

(a)

(b)

FIG. 10. Comparison of the SGS eddy-viscosity distributions evaluated in an *a priori* test with the reference data: (a) mSMM [i.e., SMM with $\Delta = (\Delta x \Delta y \Delta z)^{1/3}$] and (b) mSM [i.e., SM with $\Delta = \max(\Delta x, \Delta y, \Delta z)$].

TABLE III. Comparison of the reattachment length (X_R/H) and the secondary separation point (X_S/H) for the BSC using the mSMM.

Case	Exp.[27]	BSCmSMM
X_R/H	6.51	7.43 (+14.1%)
X_S/H	1.70	1.82

evaluating it algebraically. It, therefore, seems very useful to evaluate k_{SGS} using several algebraic models with the present highly resolved LES data. In this section, we investigate the model performance for providing k_{SGS} particularly in the shear layer downstream of the step. For this purpose, four SGS models are tested: the SM, mSM, BRD, and mLND. The latter two scale-similarity models calculate k_{SGS} using Eqs. (8) and (11), respectively.

Meanwhile, we evaluate k_{SGS} for the SM and mSM in the following manner. If we consider that both the conventional linear EVM in Eq. (4) and the one-equation SGS model in Eq. (14) provide the same value for ν_{SGS}, it holds that

$$(C_S f_S \Delta)^2 \sqrt{2S^2} = C_{SGS} f_{SGS} \sqrt{k_{SGS}} \, \Delta. \qquad (18)$$

Thus, k_{SGS} can be evaluated as

$$k_{SGS} = \left\{ \frac{(C_S f_S)^2}{C_{SGS} f_{SGS}} \right\}^2 \Delta^2 (2S^2) = 0.08 \left(\frac{f_S^4}{f_{SGS}^2} \right) \Delta^2 S^2, \qquad (19)$$

where $C_S = 0.1$ and $C_{SGS} = 0.05$. The damping functions f_S and f_{SGS} are modeled as

$$f_S = \sqrt{1 - \exp\left\{ -\left(\frac{y^+}{A}\right)^3 \right\}}, \quad f_{SGS} = 1 - \exp\left\{ -\left(\frac{y^+}{A}\right)^2 \right\}, \qquad (20)$$

where $A = 25$. Note that considering the correct near-wall limiting behavior, we adopt a well-known alternative model for f_S that is a little different from the original model in Eq. (4). Additionally, f_{SGS} is simply modeled by introducing the same parameter as used in f_S. These functions are not calibrated well and still include y^+ based on the friction velocity, and there, thus, remains a concern in using them for a separated flow. In this section, however, we focus mainly on the model performance in the shear layer at $y/H \sim 0$ downstream of the step, and these functions, thus, do not cause any crucial problem on the following discussion on an *a priori* test.

Figure 12 compares the distributions of k_{SGS} predicted by the aforementioned four SGS models with the reference data. The results of the SM in Fig. 12(a) have a trend similar to those for ν_{SGS} in Fig. 9(a). The predicted values are considerably suppressed in the shear-layer region ($y/H \sim 0$), where high aspect-ratio grid nodes are used. In contrast, the mSM provides reasonable distributions in Fig. 12(b) that generally correspond well to the reference data. Concerning the BRD and mLND, both results are generally in good agreement with the reference data.

Meanwhile, Fig. 13 shows the distributions of instantaneous k_{SGS} obtained in an *a priori* test. A comparison of these results with the reference data in Fig. 8(a) shows that the SM in Fig. 13(a) returns considerably small values in the shear-layer region. In contrast, as seen in
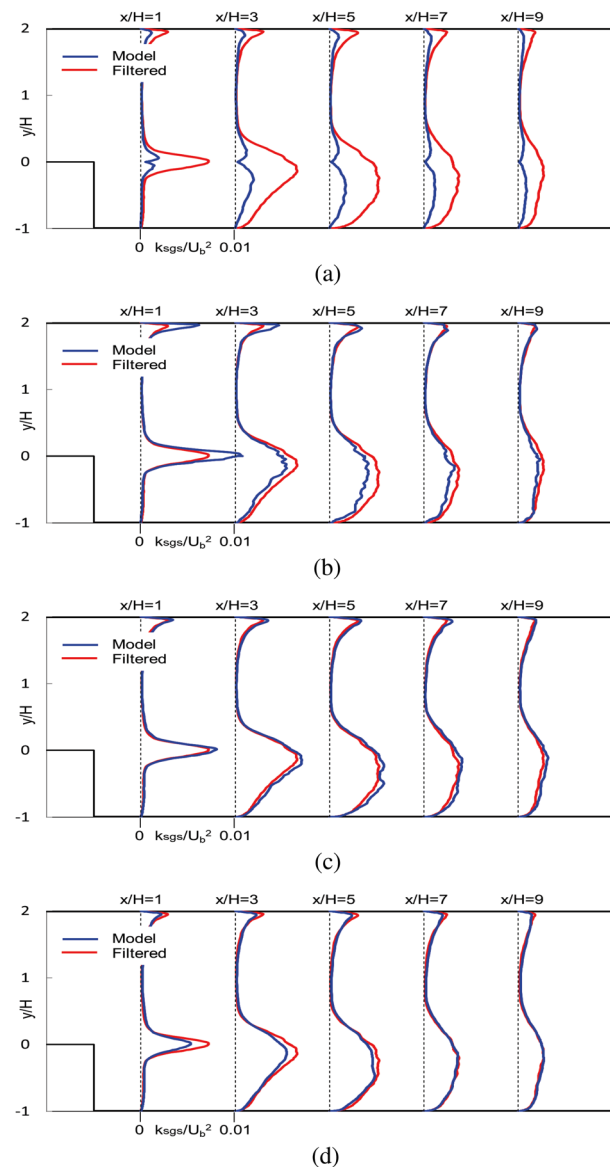
FIG. 12. Comparison of the SGS turbulence-energy distributions evaluated in an *a priori* test with the reference data: (a) SM, (b) mSM, (c) BRD, and (d) mLND.

Fig. 13(b), the mSM performs much better, although the predicted distribution still differs from the distribution of the reference data. This finding may support that an alternative option of the filter width (e.g., $\Delta = \max(\Delta x, \Delta y, \Delta z)$) is rather suitable for the LES of complex turbulence, even when including grid cells having high aspect ratios.

As for the scale-similarity models, both the BRD and mLND generally give good predictions, although some discrepancies remain in the distributions between the scale-similarity models and reference data. Careful investigation of the local distributions in Fig. 13 shows that the results of the mLND correspond best to the reference data. This may be a natural consequence of the fact that the SGS stresses of
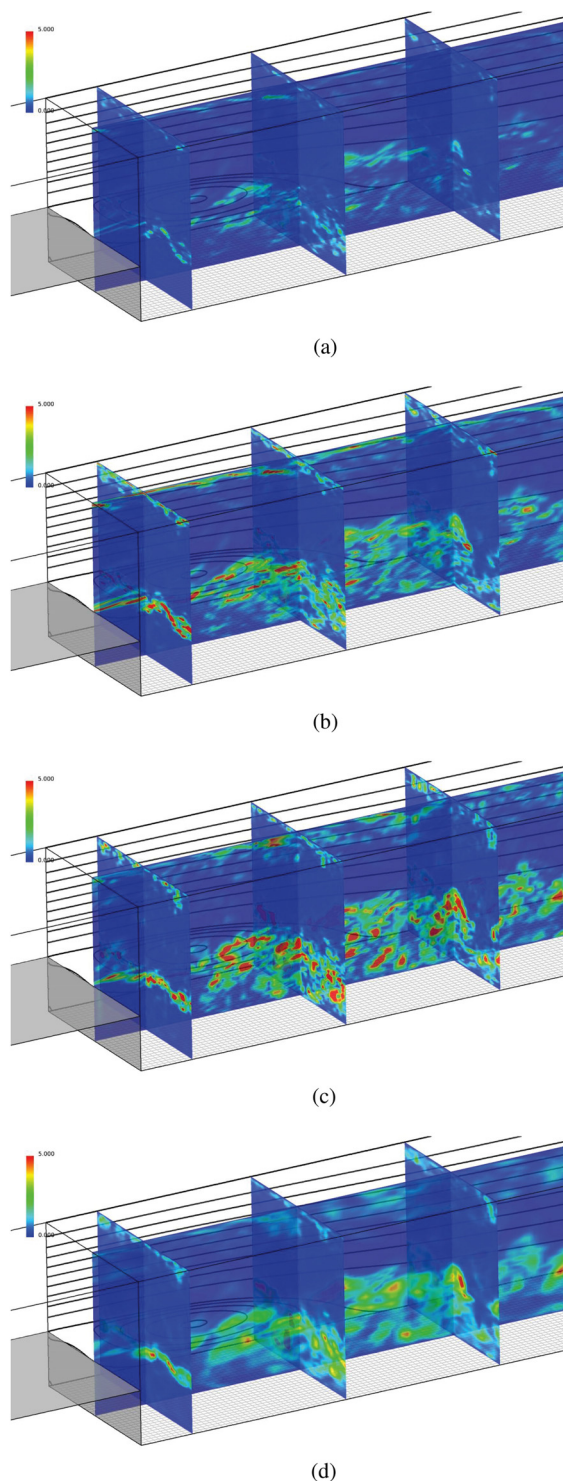
FIG. 13. Comparison of the instantaneous distributions of SGS turbulence energy for the BSC evaluated in an *a priori* test (where the color range is 0 (blue) < k_{SGS}^+ < 5 (red), normalized by the wall parameters in the driver channel): (a) SM, (b) mSM, (c) BRD, and (d) mLND.

the mLND generally have high correlation coefficients with the true SGS stresses.

V. CONCLUDING REMARKS

We investigated the effect of the definition of the filter width on the prediction accuracy of an SGS model. For this purpose, we performed *a priori* tests using the highly resolved LES data of a backstep flow that has strong shear strain as well as massive flow separation behind the step.

First, we conducted an unsteady flow simulation with a sufficiently fine grid for a backstep flow that corresponds to the experiment of Kasagi and Matsunaga.[27] We also calculated the same flow with coarser grid resolutions to compare the results with the fine-grid data. The comparison indicates that the anisotropy-resolving SGS model of Abe[14] (SMM) used in these calculations generally works well, although there remains a room to be further improved for complex turbulence.

Next, toward the further development of an SGS model, we investigated the model performance of several representative SGS models by conducting an *a priori* test using the fine-grid data. We focused on the model performance in the shear layer downstream of the step, where there exists a strong velocity gradient and the aspect ratio of a grid cell is high despite the region being far from wall surfaces. This investigation enabled us to distinguish the effect of the grid aspect ratio from the effect of near-wall damping.

For this purpose, we decomposed the fine-grid data into the GS and SGS components for a coarse-grid resolution through grid-filtering using the top-hat filtering operator. We regarded these decomposed data as the "reference data" for the corresponding grid resolution. We performed an *a priori* test for several SGS models and compared the results with the reference data. Important knowledge obtained in this work is that the cube root of a grid-cell volume is not always appropriate for the filter width used in an SGS model. To evaluate an SGS model more properly, the effect of a grid width in one direction much smaller than in other directions must be excluded in determining the filter width.

Although the SMM of Abe[14] is promising among the SGS models tested in this work, even its performance is far from perfect for complex turbulence. A better prediction of k_{SGS} may, thus, be necessary to improve the prediction accuracy. Furthermore, to reduce the computational cost, k_{SGS} is expected to be evaluated using an algebraic model. Although the *a priori* test in this work indicates that scale-similarity models can properly evaluate k_{SGS} for complex turbulence with flow separation, we also know that a pure scale-similarity model often causes numerical instability. Additionally, we showed in our previous study[14] that k_{SGS} evaluated by the BRD did not always work well for coarse-grid resolutions in an *a posteriori* test. This was why the one-equation SGS model was introduced in the current SMM.[14] Recently, however, Inagaki and Kobayashi[34] reported that an algebraic model for k_{SGS} that assumes a local equilibrium [i.e., production ∼dissipation in Eq. (15)] has a possibility of working well even for coarse-grid resolutions. Note that this assumption yields a formulation similar to that of the mSM tested in this work. It is expected that further research will enable an algebraic model to provide a much more reasonable prediction of k_{SGS} for complex turbulence in the near future, although we should also solve an important problem on the near-wall treatment that was not our main concern in this work.

AUTHOR DECLARATIONS

Conflict of Interest

The authors have no conflicts to disclose.

DATA AVAILABILITY

The data that support the findings of this study are available from the corresponding author upon reasonable request.

APPENDIX A: HYBRID LES/RANS MODEL USED IN THIS STUDY

We briefly describe the LES/RANS switching function used in the present HLR model,[28] where a new idea is proposed for connecting the LES and RANS regions. Originally, the HLR model is a turbulence model that uses LES in the region far from the wall; the modeling is then connected with RANS in the near-wall region. One strategy for connecting the LES and RANS regions is the following hybrid approach:

$$\phi = (1 - f_{hb})\,\phi_{(RANS)} + f_{hb}\,\phi_{(LES)}, \qquad (A1)$$

where ϕ is a flow variable and f_{hb} is a switching function modeled as

$$f_{hb} = 1 - \exp\left\{ -\left(C_{hb}\,\frac{l_{KL}}{\Delta} \right)^3 \right\}, \qquad (A2)$$

where C_{hb} is the model constant. In Eq. (A2), a new length scale l_{KL} is introduced instead of the simple wall distance y, that is given by

$$l_{KL} = \frac{1}{C_{KL}^{3/2}\,f_{KL}}\,\frac{k^{3/2}}{\varepsilon}, \quad f_{KL} = 1 - \exp\left\{ -\left(\frac{\sqrt{k}\,y}{C_{KL}\,\nu} \right)^{3/2} \right\}, \quad (A3)$$

where C_{KL} is the model constant and f_{KL} is the model function.

The length scale l_{KL} is originally based on that of an energy-containing eddy with some modifications by introducing knowledge of the Kolmogorov microscale, which is thought to be reasonable for representing near-wall turbulence. The algebraic model for ε is

$$\varepsilon = f_{eq}\,\frac{k^{3/2}}{2.5y} + \frac{2\nu k}{y^2}, \quad f_{eq} = 1 - \exp\left\{ -\left(\frac{\sqrt{k}\,y}{50\,\nu} \right)^2 \right\}, \quad (A4)$$

where f_{eq} is a damping function introduced to adjust the near-wall distribution of ε.

A notable feature of the present switching function f_{hb} that distinguishes this model from other previous models is in guaranteeing a full LES under a sufficiently fine grid-resolution condition. In fact,
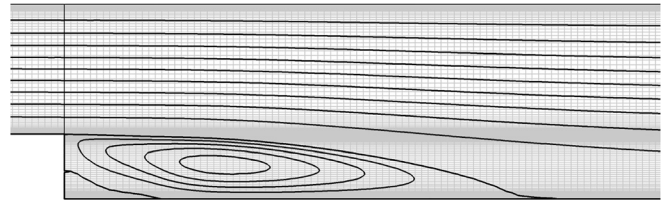

FIG. 14. Streamlines for the BSC with no SGS model.

as the grid resolution becomes finer, f_{hb} automatically approaches 1 for the whole flow field. A further detailed description of the present HLR model was given by Abe.[28]

APPENDIX B: CONFIRMATION OF THE PREDICTION ACCURACY WITH NO SGS MODEL

In this study, a sufficiently fine grid resolution is adopted for the BSF case, and the effect of the SGS model, thus, becomes so small that the results can be approximately regarded as DNS data. Meanwhile, to confirm the effect of the SGS model on the prediction accuracy for coarse grid resolutions, we perform a calculation with no SGS model for the BSC (BSCnoSGS, hereinafter).

Figure 14 shows the streamlines for the BSCnoSGS, whereas Table IV compares the reattachment length (X_R/H) and the secondary separation point (X_S/H). It is seen that the predicted separation bubble is much longer than that predicted by the SMM. Recently, many research groups have adopted the ILES in which no SGS model is included explicitly. However, as the grid resolution becomes coarser, the performance of the ILES suddenly decreases.[19] This trend is also seen in the present results, and it is, thus, preferable to introduce a high-quality SGS model for improving the prediction accuracy in the case of coarse grid resolutions.

APPENDIX C: COMPARISON OF TWO- AND THREE-DIMENSIONAL GRID-FILTERING PROCESSES

We apply the filtering operator in the x- and z-directions using a uniform grid spacing. However, one may question how the filtering operation in the y-direction affects evaluated SGS values. To answer this question, we compare the SGS values evaluated by two (x and z) and three (x, y, and z) dimensional grid-filtering processes. Although the present *a priori* test adopts a top-hat filtering operator in a real space that is applicable to any filter width in the case of uniform grid spacing, we have to be careful of applying this operation in an inhomogeneous direction.

TABLE IV. Comparison of the reattachment length (X_R/H) and the secondary separation point (X_S/H) for the BSC with no SGS model.

Case	Exp.[27]	BSCnoSGS
X_R/H	6.51	7.60 (+16.7%)
X_S/H	1.70	1.50

Therefore, in this section, we apply an alternative filtering operator based on the trapezoidal rule for all directions. The one-dimensional formulation is

$$\overline{\phi}_i = \frac{1}{4}(\phi_{i+1} + 2\phi_i + \phi_{i-1}) = \phi_i + \frac{1}{4}(\phi_{i+1} - 2\phi_i + \phi_{i-1}), \quad (C1)$$

where ϕ is a flow variable and the subscripts $i+1$, i, and $i-1$ are one-dimensional grid-node indexes. Although this formulation can be used even in an inhomogeneous direction, it is based on the trapezoidal rule, and the filter width should, thus, not exceed the stencil width in Eq. (C1). Therefore, in this evaluation, we use the results of the BSM for calculating the SGS stresses for the BSC. Although the quality of these results is a little inferior to that of the results obtained from the BSF, we can at least understand how the filtering operation in the y-direction affects the evaluated SGS values.

Figure 15 compares the SGS components for the BSC obtained from the BSM results when using a three (x, y, and z) dimensional grid-filtering operator with those when using a two (x and z) dimensional grid-filtering operator. It is seen that the two distributions have a similar trend regardless of the consideration of the y-direction. In particular, almost the same values are obtained in the shear-layer region that is the primary concern in this work. Generally, as the grid width in a direction becomes narrower, its effect on the SGS values tends to become weaker than those in the other directions with larger grid widths. In this sense, the trend in Fig. 15 is a natural consequence of the grid spacing used in this work. However, we have to keep in mind that the expression in Eq. (C1) may not be unique in an inhomogeneous direction. Therefore, to avoid ambiguity, the present work applies the filtering operator in the x- and z-directions, for which the grid spacing is uniform,

after we confirm that the filtering operation in the y-direction does not suppress the SGS values, at least, in the shear-layer region as seen in Fig. 15.

REFERENCES

[1]J. Smagorinsky, "General circulation experiments with the primitive equations: I. The basic experiment," Mon. Weather Rev. **91**, 99–164 (1963).

[2]J. Bardina, J. H. Ferziger, and W. C. Reynolds, "Improved subgrid scale models for large eddy simulation," AIAA Paper No. 80-1357, 1980.

[3]M. Germano, "A proposal for a redefinition of the turbulent stresses in filtered Navier-Stokes equations," Phys. Fluids **29**, 2323–2324 (1986).

[4]M. Germano, U. Piomelli, P. Moin, and W. H. Cabot, "A dynamic subgrid-scale eddy viscosity model," Phys. Fluids A **3**, 1760–1765 (1991).

[5]D. K. Lilly, "A proposed modification of the Germano subgridscale closure method," Phys. Fluids A **4**, 633–635 (1992).

[6]K. Horiuti, "A proper velocity scale for modeling subgrid-scale eddy viscosities in large eddy simulation," Phys. Fluids A **5**, 146–157 (1993).

[7]Y. Zang, R. L. Street, and J. R. Koseff, "A dynamic mixed subgrid-scale model and its application to turbulent recirculating flows," Phys. Fluids A **5**, 3186–3196 (1993).

[8]B. Vreman, B. Geurts, and H. Kuerten, "On the formulation of the dynamic mixed subgrid-scale model," Phys. Fluids **6**, 4057–4059 (1994).

[9]M. V. Salvetti and S. Banerjee, "A priori tests of a new dynamic subgridscale model for finite difference large eddy simulations," Phys. Fluids **7**, 2831–2847 (1995).

[10]K. Horiuti, "A new dynamic two-parameter mixed model for large-eddy simulation," Phys. Fluids **9**, 3443–3464 (1997).

[11]F. Sarghini, U. Piomelli, and E. Balaras, "Scale-similar models for large-eddy simulations," Phys. Fluids **11**, 1596–1607 (1999).

[12]Y. Morinishi and O. V. Vasilyev, "A recommended modification to the dynamic two-parameter mixed subgrid scale model for large eddy simulation of wall bounded turbulent flow," Phys. Fluids **13**, 3400–3410 (2001).

[13]M. Inagaki, "A new wall-damping function for large eddy simulation employing Kolmogorov velocity scale," Int. J. Heat Fluid Flow **32**, 26–40 (2011).

[14]K. Abe, "An improved anisotropy-resolving subgrid-scale model with the aid of a scale-similarity modeling concept," Int. J. Heat Fluid Flow **39**, 42–52 (2013).

[15]K. Abe, "An investigation of SGS-stress anisotropy modeling in complex turbulent flow fields," Flow, Turbul. Combust. **92**, 503–525 (2014).

[16]A. Vollant, G. Balarac, and C. Corre, "A dynamic regularized gradient model of the subgrid-scale stress tensor for large-eddy simulation," Phys. Fluids **28**, 025114 (2016).

[17]S. Rezaeiravesh and M. Liefvendahl, "Effect of grid resolution on large eddy simulation of wall-bounded turbulence," Phys. Fluids **30**, 055106 (2018).

[18]M. Ma, W.-X. Huang, and C.-X. Xu, "A dynamic wall model for large eddy simulation of turbulent flow over complex/moving boundaries based on the immersed boundary method," Phys. Fluids **31**, 115101 (2019).

[19]K. Abe, "Notable effect of the subgrid-scale stress anisotropy on mean-velocity prediction through budget of the grid-scale Reynolds-shear stress," Phys. Fluids **31**, 105103 (2019).

[20]K. Inagaki and H. Kobayashi, "Role of various scale-similarity models in stabilized mixed subgrid-scale model," Phys. Fluids **32**, 075108 (2020).

[21]F. X. Trias, A. Gorobets, M. H. Silvis, R. W. C. P. Verstappen, and A. Oliva, "A new subgrid characteristic length for turbulence simulations on anisotropic grids," Phys. Fluids **29**, 115109 (2017).

[22]S. T. Bose, P. Moin, and D. You, "Grid-independent large-eddy simulation using explicit filtering," Phys. Fluids **22**, 105103 (2010).

[23]S. Hickel, C. P. Egerer, and J. Larsson, "Subgrid-scale modeling for implicit large eddy simulation of compressible flows and shock-turbulence interactions," Phys. Fluids **26**, 106101 (2014).

[24]L. Guedot, G. Lartigue, and V. Moureau, "Design of implicit high-order filters on unstructured grids for the identification of large-scale features in large-eddy simulation and application to a swirl burner," Phys. Fluids **27**, 045107 (2015).

[25]F. Orley, T. Trummler, S. Hickel, M. S. Mihatsch, S. J. Schmidt, and N. A. Adams, "Large-eddy simulation of cavitating nozzle flow and primary jet break-up," Phys. Fluids **27**, 086101 (2015).

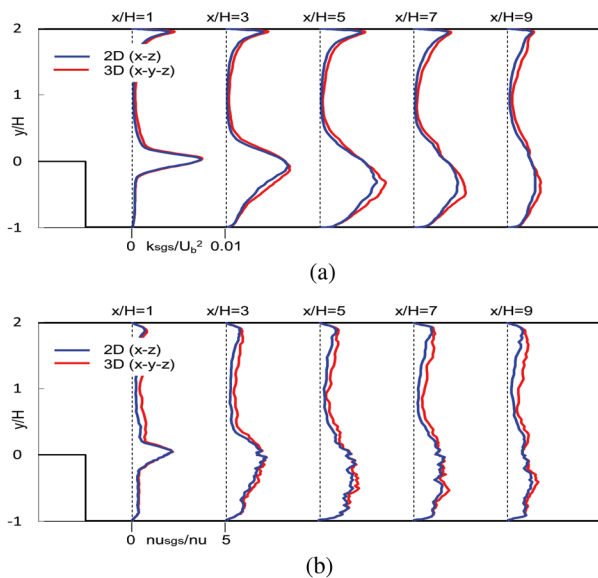FIG. 15. Comparison of the SGS components for the BSC obtained from the BSM results when using a three (x, y, and z) dimensional grid-filtering operator with those when using a two (x and z) dimensional grid-filtering operator: (a) SGS turbulence energy and (b) SGS eddy viscosity.

[26]R. Wang, F. Wu, H. Xu, and S. J. Sherwin, "Implicit large-eddy simulations of turbulent flow in a channel via spectral/hp element methods," Phys. Fluids **33**, 035130 (2021).

[27]N. Kasagi and A. Matsunaga, "Three-dimensional particle-tracking velocimetry measurement of turbulence statistics and energy budget in a backward-facing step flow," Int. J. Heat Fluid Flow **16**, 477–485 (1995).

[28]K. Abe, "An advanced switching parameter for a hybrid LES/RANS model considering the characteristics of near-wall turbulent length scales," Theor. Comput. Fluid Dyn. **28**, 499–519 (2014).

[29]M. Muto, M. Tsubokura, and N. Oshima, "Negative Magnus lift on a rotating sphere at around the critical Reynolds number," Phys. Fluids **24**, 014102 (2012).

[30]J. Kim and P. Moin, "Application of a fractional-step method to incompressible Navier-Stokes equations," J. Comput. Phys **59**, 308–323 (1985).

[31]A. A. Amsden and F. H. Harlow, "A simplified MAC technique for incompressible fluid flow calculations," J. Comput. Phys **6**, 322–325 (1970).

[32]C. M. Rhie and W. L. Chow, "Numerical study of the turbulent flow past an airfoil with trailing edge separation," AIAA J. **21**, 1525–1532 (1983).

[33]K. Abe, "Performance of a hybrid LES/RANS model combined with a wall function for predicting quite high Reynolds-number turbulent channel flows up to $Re_\tau = 6 \times 10^7$," J. Therm. Sci. Technol. **15**, JTST0014 (2020).

[34]K. Inagaki and H. Kobayashi, "Investigation on an algebraic expression of SGS turbulence energy in stabilized mixed model," in Proceedings of the 34th CFD Symposium, Japan, Paper No. A03-2, 2020).